Continuum-Scale Modeling of Helium Bubble Bursting Under Plasma-Exposed Tungsten Surfaces

Sophie Blondel[1], David E. Bernholdt[2], Karl D. Hammond[3,4], and Brian D. Wirth[1,5]

[1] Department of Nuclear Engineering, University of Tennessee, Knoxville, TN 37996-2300

[2] Computer Sciences and Mathematics Division, Oak Ridge National Laboratory, Oak Ridge, TN 37831

[3] Department of Chemical Engineering, University of Missouri, Columbia, MO 65211

[4] Nuclear Engineering Program, University of Missouri, Columbia, MO 65211

[5] Fusion and Materials for Nuclear Systems Division, Oak Ridge National Laboratory, Oak Ridge, TN 37831

Abstract - We present a comparison between a continuum-scale drift-diffusion-reaction cluster dynamics prediction of helium retention in low-energy helium plasma exposed tungsten and experimental measurements, in a temperature regime that did not produce tungsten fuzz. Our cluster dynamics model, Xolotl, has been successfully benchmarked to high helium implantation flux MD simulations at relatively low implanted fluence. In this article, we also describe the extension of the Xolotl DDR model to incorporate the effect of bubble bursting, which is observed in very high rate MD simulations, as well as MD simulations at longer times than simulated in our prior benchmarking comparison. The bursting model parameters have been tuned by comparing to MD simulations at a flux of 5.0×10^{27} m^{-2} s^{-1}, and also compared to lower implanted fluence simulations performed at ~4.0×10^{25} m^{-2} s^{-1}. This article then reports on the consistency of the Xolotl predictions with respect to the size of the simulated cluster phase space (i.e., the maximum cluster size), initial vacancy concentration, and bubble growth trajectory (maximum number of helium atoms per vacancy). Finally, our simulation results are compared to helium plasma experiments that did not produce fuzz. While the Xolotl predictions including bubble bursting are in quantitative agreement with high-flux MD simulations, the initial comparison to plasma exposure experiments at a flux on the order of 10^{21} m^{-2} s^{-1} disagree by more than an order of magnitude, and in fact cannot reproduce the trends in helium retention with varying exposure temperature. Modifying the initial vacancy concentrations and helium cluster diffusion behavior in Xolotl leads to a reasonable agreement with the experimental observations, although the underlying physical explanation for these modifications remains unclear. The predicted helium content at experimentally relevant fluxes has been shown to be relatively insensitive to the parameters used in the bubble bursting model implemented in Xolotl, although these parameters have a larger influence at higher flux. More systematic comparisons between the modeling predictions with both

experiments and MD simulation results is expected to improve the bubble bursting model in Xolotl in the future.

1. Introduction

Tungsten (W) is the leading candidate material for the divertor of next generation tokamaks such as ITER. The divertor will have to endure a harsh environment while extracting the heat produced by the fusion reaction. Tungsten was selected because of its high melting point, high thermal conductivity, low sputtering yield, and low tritium retention [1,2]. However, studies performed in linear plasma devices, as well as tokamaks using helium plasmas, have shown that low-energy helium (He) implantation (approximately 30–250 eV [3]) causes the formation of nanoscale-to-microscopic features known as “fuzz” or “coral” [3–8] that dramatically change the surface morphology and density, and can ultimately lead to enhanced erosion, degradation of material performance, and material failure. While fuzz formation has been linked to the dynamics of He atoms within tungsten through the experimental observation of He present in its tendrils [9,10], the exact formation mechanism remains unclear. However, fuzz formation has not been observed in the case of hydrogen-only plasma exposure, and thus is believed that He implantation is the cause.

Sefta and co-workers [11] demonstrated by molecular dynamics (MD) simulations that helium quickly clusters and grows into over-pressurized bubbles below the tungsten surface by repeated cycles of helium absorption and Frenkel pair formation through trap mutation and loop punching processes. Such sub-surface gas bubble growth produces surface roughening as single tungsten adatoms and prismatic dislocation loops reach the surface, in addition to the resulting surface deformation occurring when the over-pressurized gas bubbles eventually burst [11]. Ito and co-workers [12] coupled molecular dynamics and Monte Carlo simulations to model a fuzzy nanostructure in two dimensions. Their model assumed that the underlying mechanism of the formation of a fuzzy tungsten nanostructure was the ablation of tungsten by He bubbles, and then the bursting of these bubbles.

Systematic bubble evolution has also been studied, albeit at much shorter time scales, in MD simulations by Sefta and co-workers [13] to understand how bubble shape and size, temperature, the tungsten surface orientation, and the ligament thickness above the bubble influence bubble stability and surface evolution. Likewise, Hammond and co-workers [14] studied sub-surface bubble evolution in tungsten with helium implantation rates on the order of 4.0×10^{25} He m^{-2} s^{-1} and observed the bubble size and helium density evolution as well as bubble bursting. However, the time MD simulations can reach is generally limited to only a few hundred nanoseconds, with some limited simulations reaching a few microseconds, which makes comparison to actual experiments (where the fuzz takes hundreds of seconds to form) impossible.

Accelerated MD simulations using the parallel replica dynamics method, as described by Sandoval and co-workers [15], have demonstrated how the shape of a growing He bubble near the surface (1.9 nm) varies depending on the implantation rate. At high rates, like the ones used in most classical MD simulations, the bubble grows essentially isotropically and is spherical, while at lower rates, like the ones expected in ITER and those in Ref. [14], the bubble

tends to grow in an oblong shape toward the surface, leading to a bursting of the bubble earlier than if it were a spherical bubble.

While such MD, accelerated MD and coupled MD and MC simulations can provide tremendous insight into the mechanisms responsible for the observed plasma surface interactions governing tungsten surface response, these techniques are limited in the spatial and temporal scales making it difficult, if not impossible, to directly compare to experiments. To overcome the time scale limitations of classical MD simulations, we describe a drift–diffusion–reaction (DDR) cluster dynamics approach as implemented in the Xolotl simulation software [16]. Xolotl is developed within a hierarchical multiscale modeling framework, where processes and parameters observed in MD atomic-scale models are transposed to the continuum-scale. We have previously presented several benchmarks [17-19] that demonstrate the ability of our continuum model to capture the essential physical behavior and quantitatively reproduce results obtained from MD simulations. This paper describes the recent addition of a bubble bursting model to Xolotl, as well as comparing the Xolotl simulation results to experimental observations, which is the next step in being able to predict the behavior of the divertor to helium implantation in the next generation of fusion reactors.

The next section will describe both the drift-diffusion-reaction cluster dynamics approach of Xolotl itself, in addition to the model for bubble bursting. The following section focuses on comparing the results obtained by the Xolotl bursting model to MD simulations, in addition to describing Xolotl predictions of experimentally-relevant conditions, and on assessing the effects of simulation parameters on the predicted outcome. We then provide a more detailed discussion that compares our model results with experimental observations of the retained helium content in tungsten exposed to laboratory-scale plasma device. Finally, the most important conclusions of this recent development are summarized.

2. Code Description

Xolotl solves the spatially dependent DDR equations in multiple dimensions to predict the evolution of the concentration fields for a helium-implanted tungsten material. We use a finite difference implementation in which the grid along the depth direction has a variable grid size, with a finer grid near the surface, in order to better describe the profile of the incoming helium flux. In the interest of brevity, the model governing the master equations and solver will not be discussed here. These details are described in our earlier publication [19].

The clusters under consideration in this work are tungsten self-interstitials (I), vacancies (V), and helium (He), as well as vacancy-trapped helium (HeV), which we also refer to as a bubble. Single vacancies, interstitial clusters, and helium clusters are mobile and diffuse isotropically in bulk tungsten. The surface is able to move as a result of tracking the number of tungsten self-interstitial atoms diffusing to the surface and adding a grid point when this number exceeds the tungsten atomic density.

Additionally, MD simulations have revealed that the surface exerts an elastic force on mobile helium clusters that can be modeled through a biased drift term toward the surface [20,21]. In a similar way, Hu and co-workers [21,22] showed that proximity to the surface enables trap mutation reactions at sizes smaller than occur in the bulk of the material; for

instance, a cluster made of two helium atoms (He_2) can undergo trap mutation within a nanometer of the surface, but this reaction has not been observed deeper in the material. The tables used to parameterize this "modified" trap mutation are the same as discussed previously in Ref. [17]. As well, in these simulations, we have implemented an attenuation factor for this modified trap mutation, as introduced in our prior work [17], to account for the fact that the modified trap mutation reaction rates will decrease with increasing local helium content and the MD simulations which computed these reaction rates involved simulations with no pre-existing helium concentration.

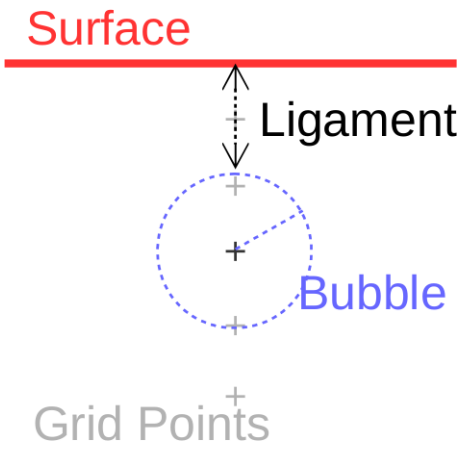

Figure 1. Schematic representation of how the ligament thickness is computed for the bubble bursting process.

As noted previously, the MD simulations exhibit bubble bursting [11–14], which occurs when a cluster of helium atoms is trapped in tungsten vacancies, grows close to the surface, resulting in the formation of an over-pressurized gas bubble that ruptures, leading to the release of the helium atoms. We have implemented a simplified model for this process in Xolotl. At the end of each time step, the total quantity of helium atoms is computed (both mobile and trapped) on each grid point, and the radius of the helium bubble, r_{n_V}, is calculated by assuming a spherical bubble that contains one vacancy for every four helium atoms (this ratio being inferred from bubble evolution in MD simulations [23]) according to:

$$r_{n_V} = r_V + \left(\frac{3\,{a_0}^3 n_V}{8\pi}\right)^{1/3} + \left(\frac{3\,{a_0}^3}{8\pi}\right)^{1/3}, \quad (1)$$

where n_V is the number of vacancies, r_V is the capture radius of a single vacancy (taken here to be $r_V = a_0\sqrt{3}/4$), and a_0 is the lattice parameter. Xolotl then calculates the ligament thickness L between the surface and the bubble diameter, based on the distance to the grid point d (depth) minus the radius of the bubble, as illustrated in Figure 1.

The bursting model implemented in Xolotl considers the bubble to have burst if the ligament thickness is zero or negative; otherwise, bursting is considered to be a stochastic phenomenon, in which a probability proportional to the ligament thickness and depth of the bubble (and including an adjustable factor) determines the probability of a bubble bursting, such that,

$$P_{bursting} \propto \left(1 - \frac{L}{d}\right) \times f \times \min(1, e^{-(d-\tau_d)/2\tau_d}). \quad (2)$$

The last term in the probability is introduced to take into account the unlikeliness of deep bubbles to burst, and τ_d is chosen here to be 10 nm. Eq. (2) is motivated by the bubble bursting analysis by Sefta and co-workers [13], which indicates that bubbles are unstable for relatively thin ligaments (shallow depths), and simplifies bubble bursting as a stochastic function of depth rather than directly calculating the bubble pressure and using a critical pressure versus depth. The distance in the simulations of Sefta and co-workers was closer to 3–5 nm, but was estimated from 'fast' MD studies. Additionally, the work of Sandoval and co-workers [15] indicates that rate effects play a role on the size/pressure of bursting, so increasing this parameter is plausible. Finally, experimental work by Miyamoto and co-workers [24] indicated bubble layer thicknesses for PISCES exposure conditions of larger than 30 nm.

When a bubble bursts in the Xolotl simulation, the concentrations of all helium clusters are set to zero at this location (grid point), and the concentrations of He_mV_n clusters are transferred to vacancy clusters of the same size (V_n). This bursting behavior mimics a pinhole bursting event, during which a cavity releases the helium but then immediately seals itself and is able to refill with incoming helium.

In order to reduce the number of equations to solve while maintaining accuracy in the results, a grouping scheme has been implemented. The main idea of this grouping scheme consists in gathering clusters with similar sizes and properties into a "super" cluster, averaging these properties, and then solving the equations for this new cluster instead of the many equations for the clusters it gathers. The approach implemented in Xolotl is the first order moment scheme as described by Kohnert and Wirth [25], but here the size of the groups is constant in terms of the number of clusters combined into a super cluster.

In order to benchmark the bursting model implemented in Xolotl, we compare Xolotl predictions to MD simulations. The large scale atomistic MD simulation was performed using the MD software LAMMPS [26], with the interactions between W atoms being described according to the embedded atom method (EAM) potential of Finnis and Sinclair [27] as modified initially by Ackland and Thetford [28] and more recently by Juslin and Wirth [29]. Tungsten–helium pairwise interactions were described according to the pair potential of Juslin and Wirth [29], and He–He interactions were described by the pair potential of Beck [30,31] as modified at short distances by Morishita and co-workers [32].

The MD simulation had a (100)-oriented free surface of 20 nm $\times$ 20 nm and a depth of 15.89 nm. Periodic boundary conditions were applied in the *x*- and *y*-directions only, that is, in the principal directions of the (horizontal) surface plane. The bottom few layers of tungsten atoms were frozen at their crystallographic coordinates to produce a quasi-reflective image stress, which prevents helium or tungsten atoms from leaving through the bottom of the box. Helium atoms were inserted at random horizontal locations and at depths sampled from a depth distribution characteristic of the (100) surface orientation at 933 K and 100 eV incident energy [33]. Helium atoms were inserted every 950 time steps, with a time step of 0.5 fs, leading to a flux of 5.0×10^{27} m^{-2} s^{-1}. We have also compared to MD simulations performed with a similar He insertion rate, but a much larger simulation cell lateral volume such that the flux is approximately 4.0×10^{25} $m^{-2}s^{-1}$. Details of similar simulations are provided in Ref. [14].

3. Results

3.1 Comparison to MD simulations

Equation (2) defines a factor used to model the bursting probability, and we have selected values for the factor f in Eq. (2) based on benchmark comparisons to MD simulations. In order to ensure that the MD simulation database included sufficient numbers of bubble bursting events, we selected an MD simulation at a high flux of 5.0×10^{27} He m^{-2} s^{-1}, which has accumulated an implanted fluence of 1.5×10^{21} He m^{-2} over the course of approximately 300 ns. We have also tested the bursting model against a MD simulation at a lower flux of 4.0×10^{27} He m^{-2} s^{-1}, with a larger simulation box of 50 nm × 50 nm × 25 nm, which only reached an implanted fluence of 4.0×10^{19} He m^{-2}. However, this MD simulation experienced much fewer bubble bursting events.

We performed simulations with Xolotl that fully reproduce the same conditions as MD within a one-dimensional slab with a thickness of 15.5 nm. The Xolotl simulation had a free surface at the (top) plasma-facing surface, along with a reflective boundary at the bottom. The incoming helium flux profile was the same as that used in the MD simulation [14, 33].

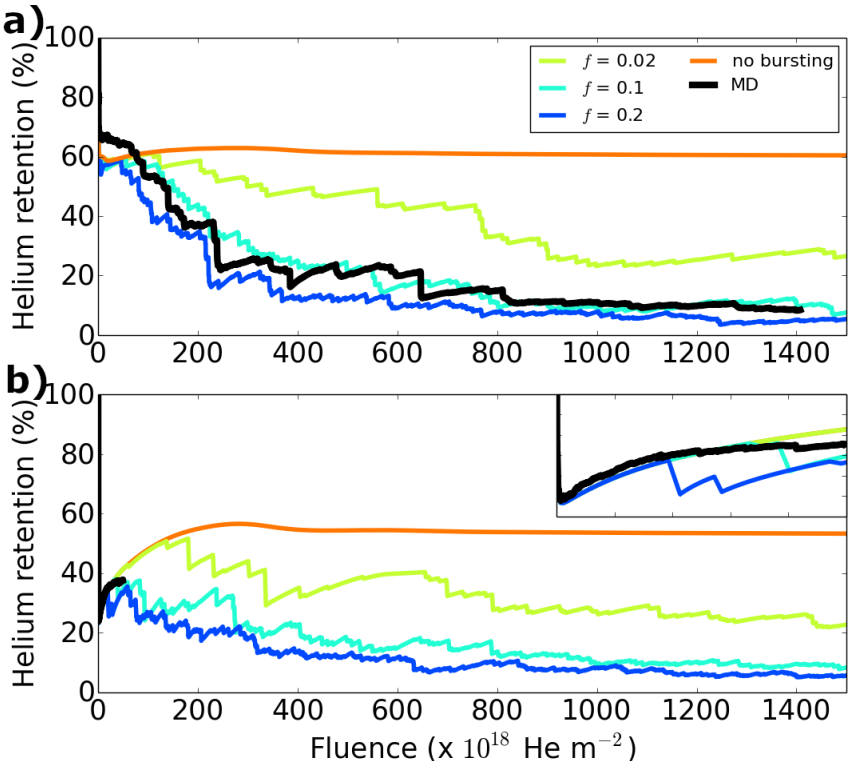

Figure 2. Percentage of helium retained in the simulation as a function of helium fluence for MD simulations and Xolotl. The Xolotl results were obtained without the bursting model as well as with three different bursting probability factors, f, as noted in the legend. The incident helium flux is a) 5.0×10^{27} He m^{-2} s^{-1} and b) 4.0×10^{25} He m^{-2} s^{-1}. Both sets of MD simulations

used a (100)-oriented tungsten surface at 933 K. The inset in b) provides a magnified view of the comparison with MD between 0 and 50×10^{18} He m^{-2} and 20 % and 50 % of retention.

Figure 2a) shows a comparison of helium retention as a function of implantation fluence as predicted by Xolotl and observed in the high flux MD simulation. Both the MD and Xolotl simulations use a helium flux of 5.0×10^{27} He m^{-2} s^{-1} incident on a (100)-oriented tungsten surface at 933 K. The sharp drops in helium retention observed in the MD simulations (black line) correspond to bubble bursting events associated with large bubbles that release substantial amounts of helium back to the plasma. Notably, the Xolotl simulation without bubble bursting grossly over-predict helium retention compared to the MD results, while the Xolotl predictions based on incorporating bubble bursting as described in Eq. (2) reproduce the sharp drops in retention. As expected, a higher value of f leads to a lower quantity of helium retained as well as more frequent drops in the distribution (bursting events). Figure 2b) presents a similar comparison at a helium implantation flux that is two orders of magnitude lower. While this MD simulation has reached a much shorter implanted fluence of 4.0×10^{19} He m^{-2} and correspondingly, fewer bubble bursting events have occurred, it is clear from the inset of Fig. 2b that the value of f = 0.1 again leads to a good agreement with the MD results. Notably, a value of f = 0.02 also provides similar agreement with the relatively low fluence MD simulations, which makes it difficult to conclusively determine the effect of implantation flux on the selected f value.

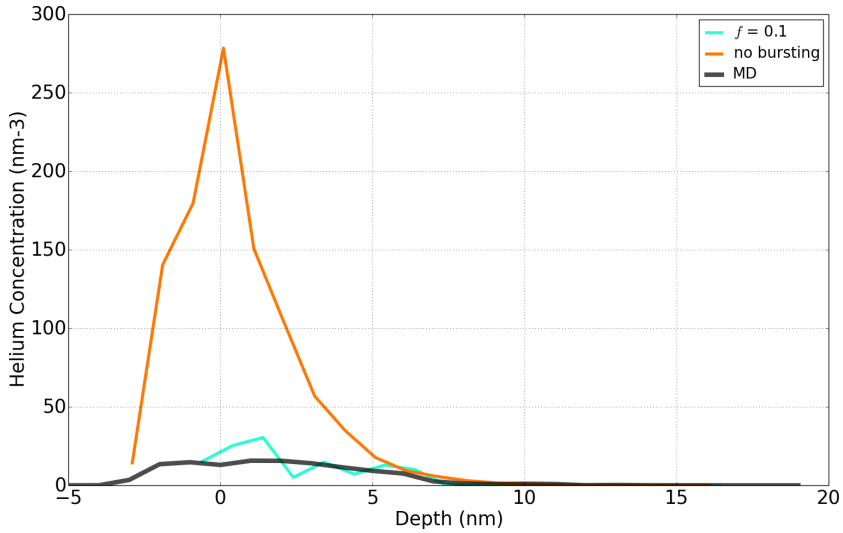

Figure 3. Predicted helium concentration as a function of depth for MD simulations (black) and Xolotl at a fluence of 1.4×10^{21} He m^{-2}. The Xolotl results were obtained both without bubble bursting (orange), as well as with a bursting probability, f of 0.1. The incident helium flux is 5.0×10^{27} He m^{-2} s^{-1} for a (100)-oriented tungsten surface at 933 K (same as Fig. 2a above). 0 nm denotes the position of the surface at t = 0 s.

Based on the comparison shown in Fig. 2a, we conclude that a value of $f = 0.1$ best reproduces the MD results, and this value will be used throughout the remainder of this article, although we return to a discussion of the effect of f value, and in particular, the flux effect later

in Section 3.3. Figure 3 presents the predicted helium concentration profile as a function of depth obtained from the higher flux MD simulations, as compared to Xolotl with and without the bursting model. The results without including sub-surface helium bubble bursting clearly overestimate the helium concentration as well as predicting a very different depth distribution than observed in the MD simulations. The Xolotl predictions with the bubble bursting model and $f = 0.1$ are in quite good agreement with the helium content and depth distribution, although Xolotl slightly underestimates the amount by which the surface has grown. It should also be noted that the size of the bubbles that are observed to burst in the MD simulation are typically larger than those modeled by Xolotl (not shown here); these discrepancies will be revisited in future publications.

With this effective benchmark of the bubble bursting model implemented in Xolotl, we next assess how different parameters impact the observables of helium retention and the helium depth distribution. We first investigate parameters that are inherent to the continuum-scale cluster dynamics simulation method, but would not exist in an actual experiment or even in MD simulations. We then discuss a comparison between Xolotl predictions of a much lower implantation flux of about 4×10^{21} He m^{-2} s^{-1} and compare with the experimental results of Woller and co-workers [34].

3.2 Effect of simulation parameters

3.2.1 Reaction network and dimensionality of solution

A considerable limitation of the cluster dynamics method is the fact that every possible cluster has to be defined, which establishes an artificial upper bound on the largest bubble in the simulation. This upper bound is dictated by memory considerations, and limits the size of the reaction network. In contrast, MD simulations directly simulate atomic interactions, allowing them to interact however the physics dictates, so there is no upper limit on the size a bubble can have, provided the simulation box is sufficiently large. By default, Xolotl considers bubbles containing up to 200 helium atoms and 50 vacancies (with a calculated radius of 5.56 Å). This maximum size is somewhat arbitrary and artificial, and can be modified to a larger value at the cost of computational memory and speed due to the larger network of equations and the corresponding Jacobian matrix that must be stored and solved. The consequence of having a finite size network is that after some time, the results of the simulation are no longer accurate: without a helium release/bubble bursting mechanism, the system of equations reaches a point of increasing concentration of the largest clusters without the ability to create even larger clusters. This leads to a steady state for the retention as can be seen in Figure 2a after a fluence of about 4×10^{20} He m^{-2} for the case not including the bursting model. However, when adding the bubble bursting process into our DDR cluster dynamics framework, the large bubbles can burst before reaching the largest size, partially removing the limitations of a finite sized domain.

In the previous section, we chose to use one spatial dimensional as an approximation to compare to MD simulation results because the only spatial dependence in the simulation conditions was regarding the depth. Xolotl has been extended to multiple dimensions [18], so it

is also possible to test how the effect of the bubble bursting is modified in two spatial dimensions.

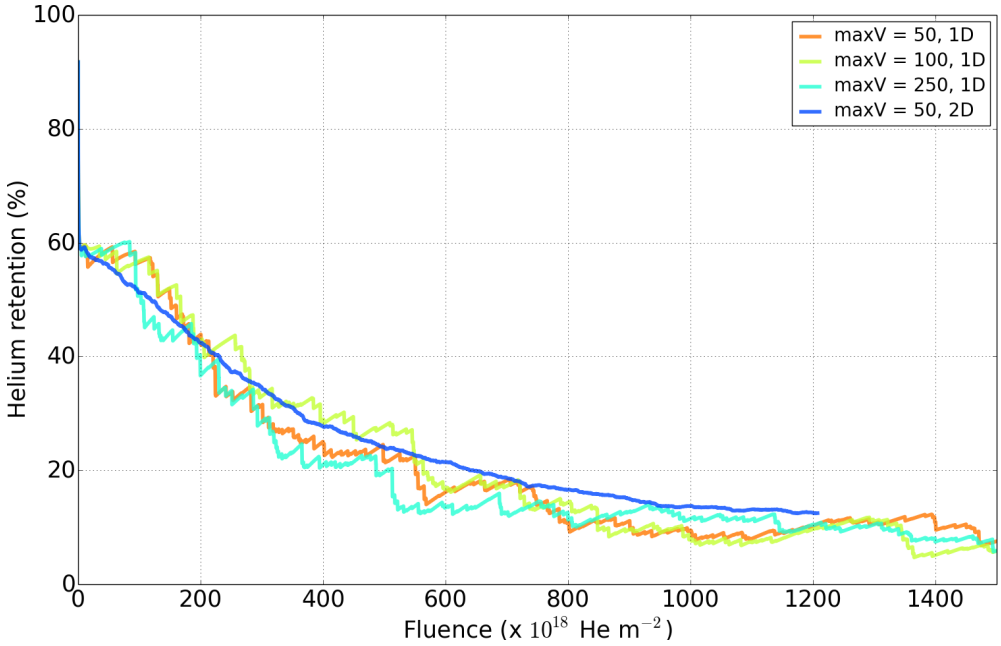

Figure 4. Percentage of helium retained as a function of helium fluence using Xolotl. The results were obtained in 1D and 2D, and with different network sizes (maxV indicates the size, *n*, of the biggest $He_{4n}V_n$ cluster). The incoming helium flux is 5.0×10^{27} He m^{-2} s^{-1} for a (100)-oriented tungsten surface at 933 K.

The impact of including additional spatial dimensions, as well as the network size, has been evaluated, and Figure 4 shows the percentage of helium retained as a function of helium fluence for four different sets of parameters involving the dimensionality of the solution domain and the maximum vacancy cluster size (the calculated radius for the biggest bubble for $He_{400}V_{100}$ is 7.06 Å, and 9.64 Å for $He_{1000}V_{250}$). It is evident from examination of Fig. 4 that the number of dimensions used to solve the problem subtly changes the helium retention. This can be explained by the fact that in two dimensions, many more bursting events happen, but each of them frees a smaller quantity of helium relative to the total fluence, leading to a smoother curve of helium retention in 2D than in 1D but following the same general trend of decreasing retention with increasing fluence. Additionally, we note that the 2D calculations are more computationally expensive than 1D calculations, which is why the 2D blue curve in Fig. 4 ends at lower accumulated fluence than the different 1D calculations (due to reaching the 24 hour wall clock simulation limit on Eos cluster within the Oak Ridge Leadership Computing Facility, OLCF). Fig. 4 also shows that the maximum reaction network size does not seem to affect helium retention significantly. The first bursting events happen when the biggest clusters with significant populations have a size around $He_{80}V_{20}$, which is much smaller than the limit even for the smaller phase space ($He_{200}V_{50}$).

For computing efficiency reasons, in the simulation results reported subsequently, we have used the smallest reaction network size ($He_{200}V_{50}$) performed using 1D (depth below the surface) simulations. We now begin a comparison to experimentally-relevant conditions, based on experiments performed by Woller and co-authors [34] that exposed tungsten disks to a 60 eV helium plasma at different fluxes and temperatures. Some of the experimental conditions led to fuzz formation [34], but here we will focus on the sub-surface He retention for the conditions that did not develop fuzz, as our simulations do not contain a model for fuzz formation. More specifically, we chose a flux of 4.4×10^{21} He m^{-2} s^{-1} at 874 K to further test the bubble bursting model, and we used the same helium implantation profile as the one computed for a (100)-oriented tungsten surface implanted with 100 eV helium. Notably, and especially at low implantation fluxes, the very small difference in implantation depth associated with 60 eV versus 100 eV helium will not significantly impact the observables of helium retention and concentration [35]. Additionally, we have to take into account the portion of helium ions that reflect from the material surface before being implanted, which was estimated as 71.1 percent by Hammond and Wirth [33].

3.2.2 Effect of the simulation depth

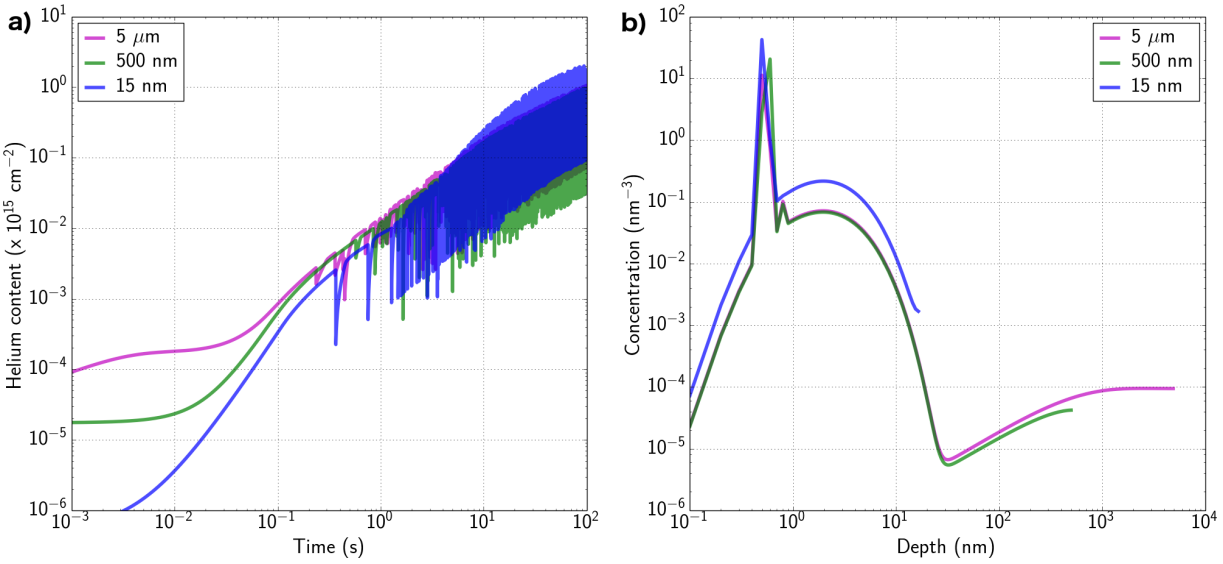

Figure 5. a) Total helium content in tungsten ($\times 10^{15}$ cm^{-2}) as a function of time (both scales are logarithmic) for different slab thickness from 15 nm to 5 μm. b) Volumetric concentration of helium (nm^{-3}) as a function of depth in nanometers (both scales are logarithmic) after 100 s of simulation. The magenta data correspond to a thickness of 5 μm, the green data to 500 nm, and the blue data to 15.5 nm. The incoming helium flux is 4.4×10^{21} He m^{-2} s^{-1} for a (100) oriented tungsten surface at 874 K.

The results presented in Figures 2a and 4 used a rather thin slab of tungsten with a thickness of 15.5 nm to compare directly to the MD simulation results. However, since we will

now compare to experimental conditions, we have extended the simulated slab thickness to either 500 nm or 5 μm to evaluate the influence of thickness on the results. Figure 5 shows both the total helium content integrated over depth as a function of time and the resulting volumetric helium concentration profile after 100 s for the three thicknesses. The helium content and concentration values presented in Fig. 5 have been obtained by integrating over all cluster sizes, including both mobile and vacancy-trapped helium. We can see that at early times (< 0.1 s), when the dominant process is diffusion, the thicker simulations retain more helium because it takes more time for the helium to diffuse to and be reflected at the mirror boundary (bottom), but once bubble nucleation process occurs (around 0.1 s), the simulation results converge independent of modeled thickness. Fig. 5b also demonstrates that the depth profiles are very similar, with a peak near the surface resulting from the helium–vacancy clusters that nucleate as a result of the modified trap mutation reactions and subsequently grow. The deeper helium concentrations have a similar shape down to about 10 nm deep, although the simulation with the thinner 15 nm thickness has a higher concentration. This is also apparent in Fig. 5a, in which the thinner 15 nm slab has a somewhat larger helium content at 100 s. The larger retained helium concentration in the thinner, 15 nm slab can be explained by the reflective boundary condition, and the close proximity of this reflective boundary to the helium implantation profile; whereas when the slab is thicker (500 nm and 5 μm), the mobile clusters diffuse deeper into the material and do not get trapped near the surface. In order to be more conservative, we chose to use the relatively thick slab of 5 μm for the remainder of the simulations in this study.

3.2.3 Effect of the initial vacancy concentration

In most of our simulations, the tungsten is considered pure and 100% dense, while most commercially-available tungsten materials contain on the order of 0.1 atom% impurities, many of which can also increase the concentration of intrinsic point defects, such as self-vacancies. Further, the tungsten divertor in fusion reactors will be subject to neutron and ion irradiation conditions that can increase the point defect populations. Consequently, we have begun to evaluate how the presence of pre-existing vacancies will influence helium bubble nucleation and helium retention behavior, again including the presence of bubble bursting. In these simulations, we are effectively using a vacancy as a proxy for any type of impurity that could interact with and bind helium. However, the interaction energetics of helium with interstitial impurities including C, N, O in W have not been calculated or determined in detail, and thus we have chosen vacancy concentration as the surrogate since the vacancy – helium interaction and binding energies are well established. As well, Yang and co-workers [36] recently evaluated the effect of the initial vacancy concentration with kinetic Monte Carlo simulations and concluded that at experimentally-relevant fluxes and temperatures, the presence of pre-existing vacancies is important to the trapping of helium clusters and has to be taken into account. Xolotl allows the setting of an initial vacancy concentration with a uniform distribution so we can test how it will influence the outcome of the simulations with bubble bursting included.

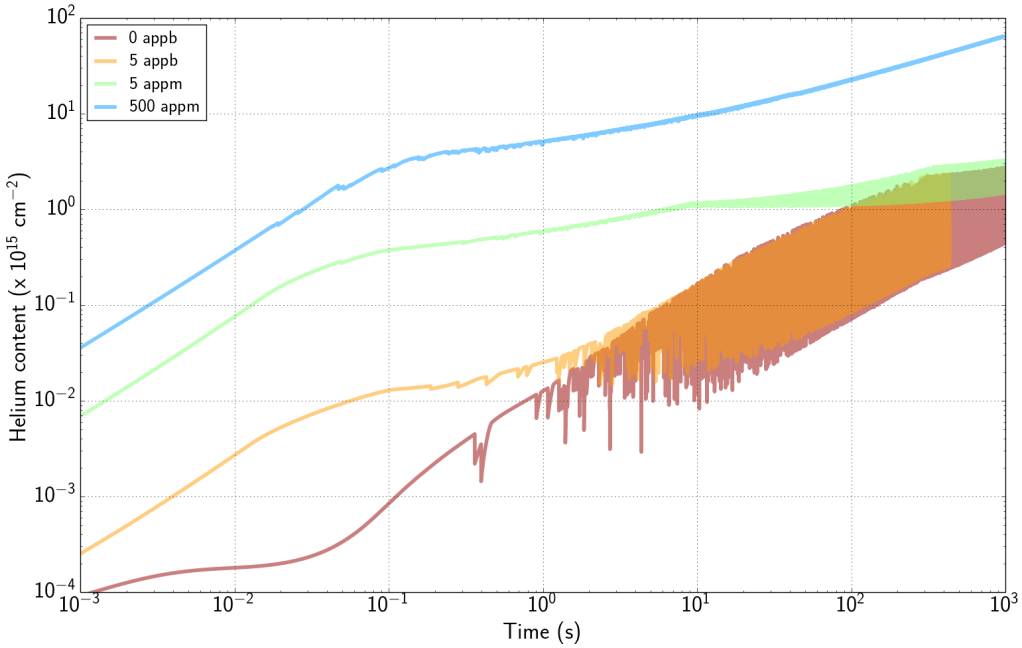

Figure 6. Total helium content retained in tungsten as a function of time for Xolotl simulations with different initial uniform concentrations of tungsten vacancy defects (both scales are logarithmic). The total incoming helium flux is 4.4×10^{21} He m^{-2} s^{-1} for a (100) oriented tungsten surface at 874 K.

Figure 6 displays the total helium content as a function of time for different concentrations of pre-existing vacancies. The vacancy formation energy of tungsten is about 3.6 eV [37], which leads to a thermal equilibrium concentration of vacancies in W at 874 K on the order of 10^{-19} per tungsten atom. Clearly, the values shown in Fig. 6 represent a sizable increase over equilibrium conditions. Again, this is because we use vacancies as a modeling proxy for impurities (carbon, oxygen, nitrogen) that are present in the material and may serve as a helium traps, and because the presence of high-energy particle irradiation (e.g., neutrons and plasma ions) is anticipated to increase the concentration of vacancies well above the equilibrium value. While the initial concentration of tungsten vacancies clearly plays an important role in the retained helium concentration and corresponding bubble nucleation at short times (< 1 s), the concentrations at later times (> 10 s) begin to converge, especially for the most likely radiation-induced vacancy concentrations between 5 appb (atomic parts per billion) and 5 appm. This presumably indicates that once bubble nucleation has completed, there is a self-similar evolution dictated by the helium bubble growth and bubble bursting phenomena.

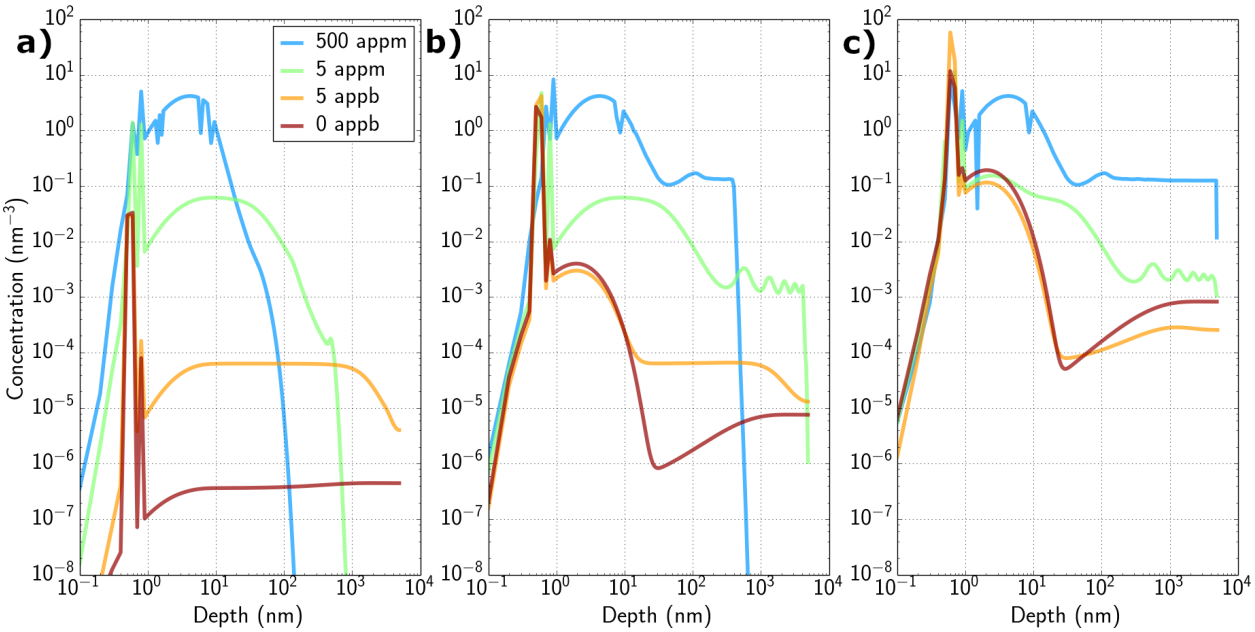

Figure 7. Total helium concentration as a function of depth for different times predicted by Xolotl (both scales are logarithmic) for a total incoming helium flux of 4.4×10^{21} He m^{-2} s^{-1} for a (100)-oriented tungsten surface at 874 K. a) corresponds to t = 0.1 s, b) to t = 7.5 s, and c) to t = 300.0 s.

The time evolution of the total helium concentration distribution as a function of depth is shown in Figure 7 for the four different initial vacancy concentrations. Each distribution displays similar characteristic peaks near the surface due to the modified trap mutation that produces a high concentration of immobile He_nV_m clusters. However, the deeper helium concentration profiles are clearly different, with more helium trapped and retained at vacancies further below the surface with increased vacancy concentration. The helium retention in the simulations with no initial vacancies and with 5 appb vacancies converge for times between about 10 and 100 seconds (as shown in Fig. 6), which is also clearly shown by the He concentration distribution as a function of depth shown in Fig. 7b-c, where the two sets of parameters yield virtually the same profile. Figure 7 also indicates the likelihood, within about another 100 seconds, that the predicted He concentration with an initial vacancy concentration of 5 appm will also converge towards the results at low initial vacancy concentration. This can be interpreted as an additional relative influence of the initial vacancy concentration on the retained helium, depending on the time scale being studied. However, from the simulation with 500 appm, there is a threshold above which the results are unlikely to converge to the results at lower vacancy concentrations within a reasonable time.

The oscillations seen at greater depths for 5 appm, and to a lesser extent for 500 appm, are due to the combination of pre-existing vacancies and diffusion. As helium diffuses deeper in the material, it gets trapped by vacancies through the He + V → HeV reaction, the vacancies that are located deeper in the material are allowed to diffuse towards the free surface, generating an excess of HeV bubble embryos at that location followed by a lack of the same embryos deeper, where the mobile vacancies came from. This process is then repeated with a

characteristic length, generating the wave-like oscillations. The initial vacancy concentration of 500 appm leads to the most apparent manifestation of these oscillations in our simulations.

3.2.4 Effect of the bubble growth trajectory

In Xolotl, we have parameterized the helium–vacancy phase space to grow along a trajectory of 4 helium per vacancy. This was based on an earlier parameterization of the helium–vacancy energetics from molecular statics simulations [23]. However, recent large-scale MD simulations with an implantation flux on the order of 4.0×10^{25} He m^{-2} s^{-1} [14] indicated that helium bubble growth trajectories, on average, can be described by a power law:

$$n_{He} = 5\, n_V^{0.86}, \tag{3}$$

where n_{He} is the number of helium contained in a cluster, or bubble, containing n_V vacancies.

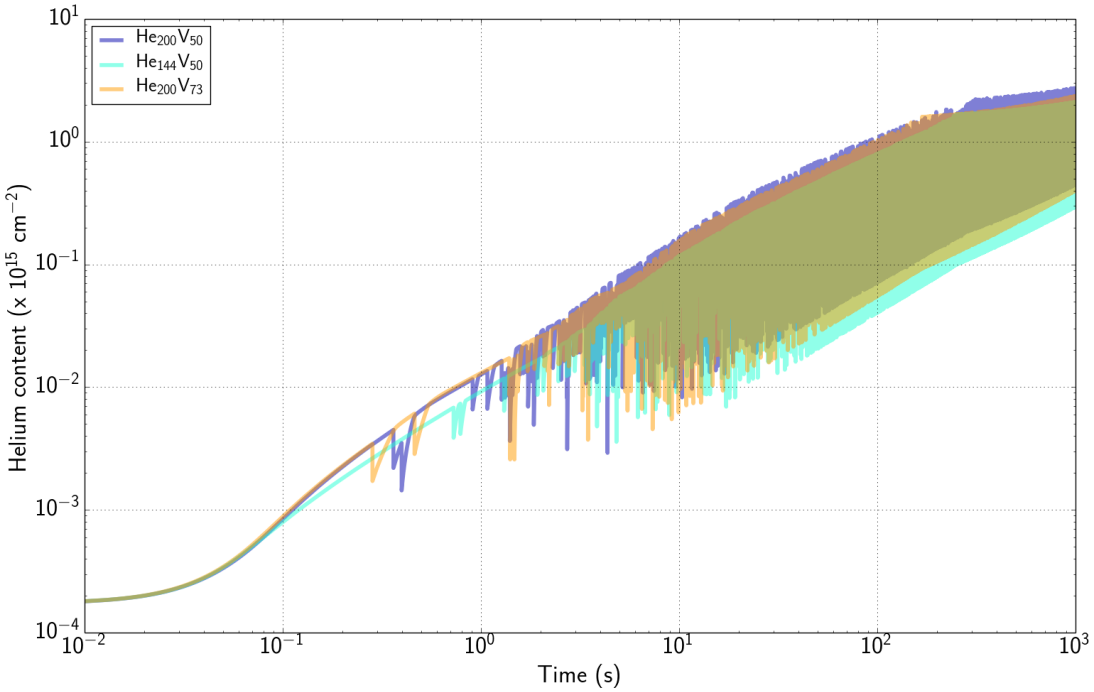

Figure 8. Xolotl predictions of total helium content in tungsten as a function of time. All predicted data result from a simulation of an incident helium flux of 4.4×10^{21} He m^{-2} s^{-1} for a (100)-oriented tungsten surface at 874 K. The dark blue data are for the standard network in Xolotl (i.e., He/V = 4), while the light blue and orange data use a network following the updated trajectory according to Eq. (3), with the blue line matching the maximum helium cluster size and the orange line matching the maximum vacancy size. The legend indicates the size of the biggest cluster included in the Xolotl model.

We re-parameterized the helium–vacancy phase space in Xolotl assuming that the growth trajectory would follow Eq. (3) instead of the constant value of 4 for the He/V ratio used in the previous results. In particular, we used two networks for which the only difference is the size of the biggest cluster: one with the same maximum size of vacancy in the clusters (biggest

cluster is $He_{144}V_{50}$) and the other one with the same maximum size of helium (biggest cluster is $He_{200}V_{73}$). We evaluated the effect of this new parameterization on the retained helium, as shown in Figure 8. While there is some scatter due to bubble bursting, all three curves follow a similar trajectory with time. We thus conclude the results are relatively insensitive to the He/V ratio.

3.3 Comparison to Experiment and Discussion

The results obtained from the bubble bursting model implemented in Xolotl were not strongly affected by varying the different simulation parameters, and tended to converge within about 100 seconds. One exception relates to the f value in Eq. (2), which we adjusted to provide good agreement with the MD simulations performed at a flux of 5.0×10^{27} $m^{-2}s^{-1}$, and to a lesser extent at a flux of 4×10^{25} $m^{-2}s^{-1}$, but which we expect should vary with implantation flux, albeit perhaps not in a simple fashion. In order to test this model, we now compare Xolotl predictions to the experiment performed by Woller and co-workers [34] at the DIONISOS linear plasma device. As described earlier, different samples of tungsten were exposed to 60 eV helium ions in a linear plasma device with varying implantation flux and sample temperature. Here, we are only interested in the conditions that did not produce fuzz, and Figure 9 shows the evolution of helium content as a function of time for three flux-temperature conditions, corresponding to specimens e, f, and g in the Woller study [34]. These three conditions involve a helium flux of 2.5×10^{20}, 4.4×10^{21} and 5.6×10^{21} $m^{-2}s^{-1}$, respectively, at 1057, 874 and 527 K.

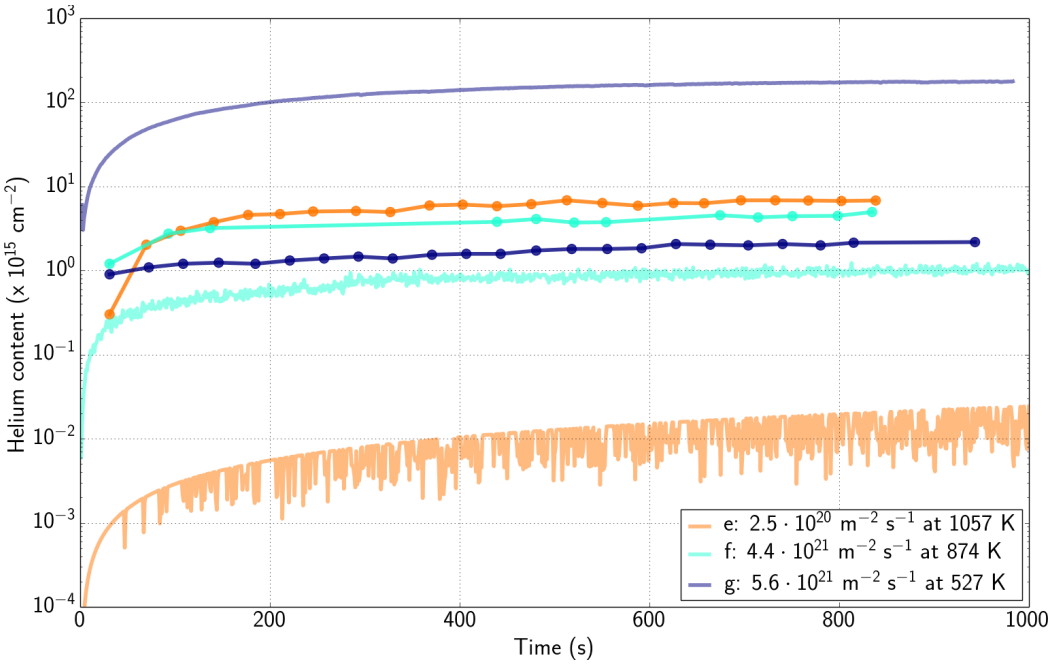

Figure 9. Total helium content in low-energy helium plasma exposed tungsten as a function of time, averaged every second, for the 3 experimental conditions (noted as e, f and g) that do not produce fuzz in Ref. [34]. The solid lines with circles show the experimental data, as reproduced from Woller and co-workers [34]. The solid lines are predicted by Xolotl with the bubble bursting model.

Figure 9 shows the integrated helium content as a function of time for these three conditions. Our model predictions are orders of magnitude away from the experimental results and show a temperature and flux dependence opposite to the measured helium content. This dependence is however consistent with other simulation predictions [23], for which lower helium retention is predicted at higher temperature [11] and more retention for higher implantation rates.

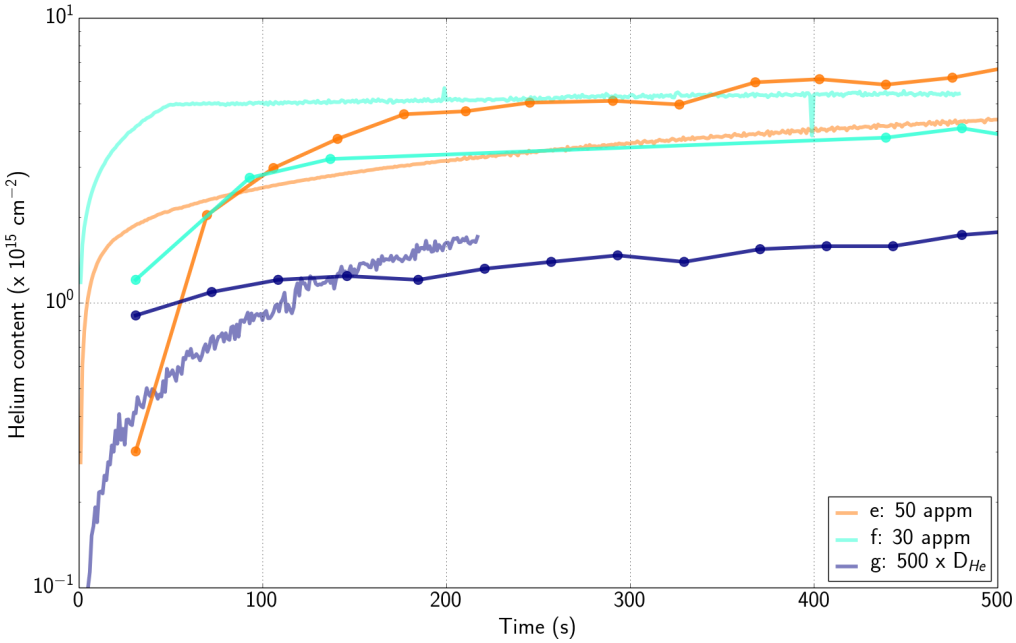

Figure 10. Total helium content in low-energy helium plasma exposed tungsten as a function of time, averaged every second, for the 3 experimental conditions (noted as e, f and g) that do not produce fuzz in Ref. [34]. The solid lines with circles show the corresponding experimental data, as reproduced from Woller and co-workers [34]. The corresponding solid lines are Xolotl predictions with bubble bursting and with modified simulation conditions that are required to provide better agreement with the experimental data. These modifications include incorporating pre-existing vacancies for the two higher temperature exposure conditions e and f (50 appm and 30 appm, respectively) and much larger diffusion coefficients for the mobile helium clusters for the lower temperature exposure condition g (all mobile cluster diffusivities multiplied by 500).

In order to improve the agreement between our simulation predictions and the experimental results, we have modified the simulation conditions. Figure 10 shows that a much better agreement can be obtained (comparisons now within ~2-3X), although it is not immediately obvious what are the physical explanations for the modified simulation conditions. For instance, increasing the initial vacancy concentration for cases e and f results in a prediction of the helium content which is of the same order of magnitude as measured in the experiments. The values of 50 appm (e) and 30 appm (f) are consistent with the presence of

higher defect concentrations at higher temperatures, although it is not obvious why the higher temperature exposure would contain more impurities. For the lower temperature case g, using diffusion coefficients for mobile helium clusters that are 500 times higher than our standard values obtained through MD simulations, decreases the helium content such that it is now within the region of the experimental measurements. The reduced retention is produced by the higher diffusivity that increases the helium diffusion back to the surface where it can be desorbed. But, again, it is not entirely clear why the helium cluster diffusivity must be higher for the lower temperature plasma exposure than the other conditions.

Finally, as discussed previously in association with Figure 2, the parameterization of the f factor within the bubble bursting model was based on comparing Xolotl predictions to MD simulations using a very high (5.0×10^{27} $m^{-2}s^{-1}$) or, to a lesser extent, a high (4.0×10^{25} $m^{-2}s^{-1}$) implantation flux. In order to compare with the experimental conditions, we have reduced the implantation flux to ~10^{21} $m^{-2}s^{-1}$, but have kept the bursting model f factor at the same value of 0.1. With decreasing flux, one can make an argument for either increasing or decreasing the f factor. On one hand, we might expect that bubbles would be deeper below the surface with a lower helium implantation flux as a result of the reduced helium retention and the longer time available for diffusion prior to encountering another helium atom or impurity leading to the critical bubble nucleation size. As shown by Sefta and co-workers [13], deeper bubbles require a larger gas pressure in order to burst, which would suggest that the f factor should decrease with decreasing helium implantation flux. On the other hand, accelerated MD simulations by Sandoval and co-workers [15] have shown that the growth rate of the bubble, which is directly linked to the incoming flux, has a strong effect on bubble evolution, and that a lower growth rate changes the bubble shape (growth in oblong fashion towards the surface) and produces bubble bursting at lower pressure containing fewer helium atoms. This could be interpreted as increasing the f factor with decreasing flux.

Thus, to assess the effect of the f factor on helium retention, we have performed additional Xolotl simulations for the e case conditions from Woller and co-workers [34] and a pre-existing vacancy concentration of 50 appm. Figure 11 presents the Xolotl predictions that result from varying the f factor, from 0.01 to 10.0. We observe that the predicted He retention is identical for an f factor of 0.01 and 0.1. Increasing the f factor to 1.0 results in a slight reduction in the retained helium content, but the results plotted in Fig. 11 indicate that the bubble bursting model is actually relatively insensitive to the value of the f factor between 0.01 and 1. With further increasing the f factor to 10, a more significant reduction in the retained He concentration are predicted.

We anticipate that further refinement of the bubble bursting model and the f factor will require additional comparisons of the Xolotl predictions to experimental results. More specifically, we believe that comparing the depth dependence of the helium concentration below the surface, as well as the size and spatial dependence of the bubble population will provide further results that can be used to improve our model. For instance, in comparing the Xolotl predictions to the MD data presented in Fig. 2a, the first bursting event is observed in the MD simulation to occur at a fluence of 2.0×10^{19} He m^{-2} for a bubble containing 116 helium atoms; whereas in the Xolotl simulation, the first bursting event occurs at 1.2×10^{19} He m^{-2} for a bubble containing 80 helium atoms.

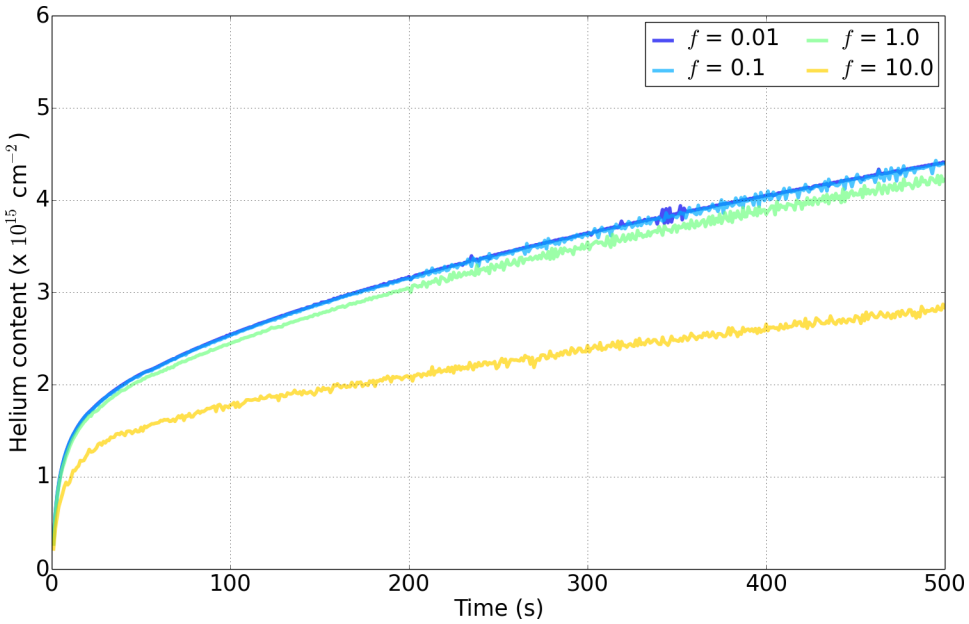

Figure 11. Total helium content in low-energy helium plasma exposed tungsten as a function of time, averaged every second, for the e case from Ref. [34], and using a pre-existing vacancy concentration of 50 appm. The solid lines are predicted by Xolotl with the bubble bursting model, in which the f factor (Eq. (2)) has been varied from 0.01 to 10.0.

Another aspect of bubble bursting that has not yet been implemented in Xolotl relates to the post-bursting evolution of the bubble. In the work reported here, we have always assumed that the bursting event happens in a pin-hole rupture that is able to re-heal, leaving a vacancy cavity that can re-fill with helium. However, MD simulations [13] have shown that some bursting events lead to the formation of a crater. In this case, the ligament of tungsten between the bubble and the surface is significantly deformed with no material left above the bubble, so that the cavity cannot refill with helium. This sort of bursting behavior was seen at high rates of bubble growth by Sefta and co-workers [13]. A way to model this behavior would be to move the surface back to where the bubble was located and reset all the concentrations in this region to zero. The surface would then be able to grow back again through the trap mutation process and the creation of adatoms. Sefta and co-workers observed in their MD simulations that the outcome of the bursting event as a pinhole or a crater depends mainly on the state of the ligament separating the bubble from the surface. If it is thin and fragile enough, it will more likely lead to a pinhole. Future publications will report on the influence of bursting mode in the Xolotl predictions.

4. Conclusion

We describe the implementation of a new bubble bursting model in the Xolotl DDR cluster dynamics code based on a pinhole model of bursting. The model quantitatively and qualitatively reproduces features of the helium retention curve obtained from an MD

simulation at a flux of 5.0×10^{27} He m^{-2} s^{-1} and 933 K; that is, a significant drop in helium retention after a bursting event, with subsequent increased retention observed as the cavity again fills with helium. It was then tested by varying simulation parameters related to the approximations within our cluster dynamics model, such as the size of the cluster reaction network, the He/vacancy growth trajectory of bubbles, the effect of pre-existing vacancy concentration and the number of spatial dimensions, and the model predictions of helium retention proved to be robust with respect to these parameters.

We next compared Xolotl predictions of helium retention to an experimental investigation performed at DIONISOS [34]. However, Xolotl does not correctly predict the temperature dependence nor the flux dependence of helium retention in tungsten observed in the experiments. Modifying the initial vacancy concentrations and helium cluster diffusion behavior in Xolotl leads to a reasonable agreement with the experimental observations, although the underlying physical explanation for these modifications remains unclear. The predicted helium content at experimentally relevant fluxes has been shown to be relatively insensitive to the parameters used in the bubble bursting model implemented in Xolotl, although these parameters have a larger influence on retention at higher flux. More systematic comparisons between the modeling predictions with both experiments and MD simulation results is expected to improve the bubble bursting model in Xolotl in the future, but we have demonstrated the ability of an atomically-informed drift-diffusion-reaction cluster dynamics model to directly compare to experiments due to the ability to reach time scales on the order of 100 seconds or more.

5. Acknowledgments

This work was supported by the U. S. Department of Energy, Office of Fusion Energy Sciences and Office of Advanced Scientific Computing Research through the Scientific Discovery through Advanced Computing (SciDAC) project on Plasma–Surface Interactions. This research used resources of the Oak Ridge Leadership Computing Facility at the Oak Ridge National Laboratory, which is supported by the Office of Science of the DOE under contract DE-AC05-00OR22725. The MD large-scale simulation used resources of the Argonne Leadership Computing Facility, which is a DOE Office of Science User Facility supported under contract DE-AC02-06CH11357, and also used resources of the National Energy Research Scientific Computing Center, a DOE Office of Science User Facility supported by the Office of Science of the DOE under contract DE-AC02-05CH11231.

Oak Ridge National Laboratory is managed by UT–Batelle, LLC for the U. S. Department of Energy under contract No. DE-AC05-00OR22725.

6. References

1. ITER: The Way to New Energy, 2012; http://www.iter.org/

2. R. Aymar, “ITER Overview,” *Fusion Eng. Des.*, 36, 9–21 (1997); https://doi.org/10.1016/S0920-3796(97)00008-2

3. K. D. Hammond, “Helium, Hydrogen, and Fuzz in Plasma-Facing Materials,” *Mater. Res. Express*, 4, 104002 (2017); https://doi.org/10.1088/2053-1591/aa8c22

4. S. J. Zenobia and G. L. Kulcinski, “Formation and retention of surface pores in helium-implanted nano-grain tungsten for fusion reactor first-wall materials and divertor plates,” *Phys. Scr.*, T138, 014049 (2009); http://dx.doi.org/10.1088/0031-8949/2009/T138/014049

5. M. Miyamoto, D. Nishijima, M. J. Baldwin, R. P. Doerner, Y. Ueda, K. Yasunaga, N. Yoshida and K. Ono, “Microscopic damage of tungsten exposed to deuterium–helium mixture plasma in PISCES and its impacts on retention property,” *J. Nucl. Mater.*, 415, S657 (2011); http://dx.doi.org/10.1016/j.jnucmat.2011.01.008

6. M. J. Baldwin, T. C. Lynch, R. P. Doerner and J. H. Yu, “Nanostructure formation on tungsten exposed to low-pressure rf helium plasmas: A study of ion energy threshold and early stage growth,” *J. Nucl. Mater.*, 415, S104 (2011); http://dx.doi.org/10.1016/j.jnucmat.2010.10.050

7. S. Kajita, N. Yoshida, R. Yoshihara, N. Ohno and M. Yamagiwa, “TEM observation of the growth process of helium nanobubbles on tungsten: Nanostructure formation mechanism,” *J. Nucl. Mater.*, 418, 152 (2011); http://dx.doi.org/10.1016/j.jnucmat.2011.06.026

8. G. M. Wright, D. Brunner, M. J. Baldwin, K. Bystrov, R. P. Doerner, B. Labombard, B. Lipschultz, G. De Temmerman, J. L. Terry, D. G. Whyte and K. B. Woller, “Comparison of tungsten nano-tendrils grown in Alcator C-Mod and linear plasma devices,” *J. Nucl. Mater.*, 438, S84 (2013); http://dx.doi.org/10.1016/j.jnucmat.2013.01.013

9. S. Kajita, S. Takamura, N. Ohno, D. Nishijima, H. Iwakiri, and N. Yoshida, “Sub-ms Laser Pulse Irradiation on Tungsten Target Damaged by Exposure to Helium Plasma,” *Nucl. Fusion* 47, 1358–1366 (2007); https://doi.org/10.1088/0029-5515/47/9/038

10. G. De Temmerman, K. Bystrov, and J. J. Zielinski, “Nanostructuring of Molybdenum and Tungsten Surfaces by Low-Energy Helium Ions,” *J. Vac. Sci. Technol.*, 30, 041306 (2012); https://doi.org/10.1116/1.4731196

11. F. Sefta, K. D. Hammond, N. Juslin, and B. D. Wirth, “Tungsten Surface Evolution by Helium Bubble Nucleation, Growth, and Rupture,” *Nucl. Fusion* 53, 073015 (2013); https://doi.org/10.1088/0029-5515/53/7/073015

12. A. M. Ito, Y. Yoshimoto, S. Saito, A. Takayama and H. Nakamura, "Molecular dynamics simulation of a helium bubble bursting on tungsten surfaces," *Phys. Scr.*, T159, 014062 (2014); http://dx.doi.org/10.1088/0031-8949/2014/T159/014062

13. F. Sefta, N. Juslin and B. D. Wirth, "Helium bubble bursting in tungsten," *J. Appl. Phys.*, 114, 243518 (2013); http://dx.doi.org/10.1063/1.4860315

14. K. D. Hammond, S. Blondel, L. Hu, D. Maroudas and B. D. Wirth, "Large-scale atomistic simulations of low-energy helium implantation into tungsten single crystals," *Acta Mater.*, 144 (2018); https://doi.org/10.1016/j.actamat.2017.09.061

15. L. Sandoval, D. Perez, B. P. Uberuaga and A. F. Voter, "Competing Kinetics and He Bubble Morphology in W," *Phys. Rev. Lett.*, 114, 105502 (2015); https://doi.org/10.1103/PhysRevLett.114.105502

16. Xolotl website: https://github.com/ORNL-Fusion/xolotl

17. S. Blondel, K. D. Hammond, L. Hu, D. Maroudas and B. D. Wirth, "Modeling Helium Segregation to the Surfaces of Plasma-Exposed Tungsten as a Function of Temperature and Surface Orientation," *Fusion Sci. Technol.*, 71 (2017); http://dx.doi.org/10.13182/FST16-112

18. S. Blondel, D. E. Bernholdt, K. D. Hammond, L. Hu, D. Maroudas and B. D. Wirth, "Benchmarks and Tests of a Multidimensional Cluster Dynamics Model of Helium Implantation in Tungsten," *Fusion Sci. Technol.*, 71 (2017); http://dx.doi.org/10.13182/FST16-109

19. D. Maroudas, S. Blondel, L. Hu, K. D. Hammond and B. D. Wirth, "Helium segregation on surfaces of plasma-exposed tungsten," *J. Phys. Condens. Matter*, 28 (2016); http://dx.doi.org/10.1088/0953-8984/28/6/064004

20. L. Hu, K. D. Hammond, B. D. Wirth and D. Maroudas, "Interactions of mobile helium clusters with surfaces and grain boundaries of plasma-exposed tungsten," *J. Appl. Phys.*, 115, 173512 (2014); http://dx.doi.org/10.1063/1.4874675

21. L. Hu, K. D. Hammond, B. D. Wirth and D. Maroudas, "Molecular-dynamics analysis of mobile helium cluster reactions near surfaces of plasma-exposed tungsten," *J. Appl. Phys.*, 118, 16, 163301 (2015); http://dx.doi.org/10.1063/1.4933393

22. L. Hu, K. D. Hammond, B. D. Wirth and D. Maroudas, "Dynamics of small mobile helium clusters near tungsten surfaces," *Surf. Sci.*, 626, L21 (2014); http://dx.doi.org/10.1016/j.susc.2014.03.020

23. T. Faney, S. I. Krasheninnikov and B. D. Wirth, “Spatially dependent cluster dynamics model of He plasma surface interaction in tungsten for fusion relevant conditions,” *Nucl. Fusion*, 55 (2015); http://dx.doi.org/10.1088/0029-5515/55/1/013014

24. M. Miyamot, S. Mikami, H. Nagashima, N. Iijima, D. Nishijima, R.P. Doerner, N. Yoshida, H. Watanabe, Y. Ueda and A. Sagara, “Systematic investigation of the formation behavior of helium bubbles in tungsten,” *J. Nucl. Mater.*, 463 (2015); https://doi.org/10.1016/j.jnucmat.2014.10.098

25. A. A. Kohnert and B. D. Wirth, “Grouping techniques for large-scale cluster dynamics simulations of reaction diffusion processes,” *Model. Simul. Mater. Sci. Eng.*, 25, 1, 015008 (2017); http://dx.doi.org/10.1088/1361-651X/25/1/015008

26. S. Plimpton, “Fast Parallel Algorithms for Short-Range Molecular Dynamics,” *J. Comput. Phys.*, 117, 1, 1 (1995); http://dx.doi.org/10.1006/jcph.1995.1039

27. M. W. Finnis and J. E. Sinclair, “A Simple Empirical N-Body Potential for Transition-Metals,” *Philos. Mag. A*, 50, 1, 45 (1984); http://dx.doi.org/10.1080/01418618408244210

28. G. J. Ackland and R. Thetford, “An Improved N-Body Semiempirical Model for Body-Centered Cubic Transition-Metals,” *Philos. Mag. A*, 56, 1, 15 (1987); http://dx.doi.org/10.1080/01418618708204464

29. N. Juslin and B. D. Wirth, “Interatomic Potentials for Simulation of He Bubble Formation in W,” *J. Nucl. Mater.*, 432, 1, 61 (2013); http://dx.doi.org/10.1016/j.jnucmat.2012.07.023

30. D. E. Beck, “A New Interatomic Potential Function for Helium,” *Mol. Phys.*, 14, 4, 311 (1968); http://dx.doi.org/10.1080/00268976800100381

31. D. E. Beck, “Erratum: A New Interatomic Potential Function for Helium,” *Mol. Phys.*, 15, 3, 332 (1968); http://dx.doi.org/10.1080/00268976800101171

32. K. Morishita, R. Sugano, B. D. Wirth and T. Diaz de la Rubia, “Thermal Stability of Helium-Vacancy Clusters in Iron,” *Nucl. Instrum. Methods Phys. Res. B*, 202, 76 (2003); http://dx.doi.org/10.1016/S0168-583X(02)01832-3

33. K. D. Hammond and B. D. Wirth, “Crystal orientation effects on helium ion depth distributions and adatom formation processes in plasma-facing tungsten,” *J. Appl. Phys.*, 116, 143301 (2014); http://dx.doi.org/10.1063/1.4897419

34. K. B. Woller, D. G. Whyte and G. M. Wright, “Dynamic measurement of the helium concentration of evolving tungsten nanostructures using Elastic Recoil Detection during

plasma exposure," *J. Nucl. Mater.*, 463, 289-293 (2015); https://doi.org/10.1016/j.jnucmat.2014.11.126

35. O. Cekmer, K. Sargsyan, S. Blondel, H. Najm, D. E. Bernholdt and B. D. Wirth, "Uncertainty quantification for incident helium flux in plasma exposed tungsten," submitted to *International Journal for Uncertainty Quantification*

36. Z. Yang, S. Blondel, K. D. Hammond and B. D. Wirth, "Kinetic Monte Carlo Simulations of Helium Cluster Nucleation in Tungsten with Preexisting Vacancies," *Fusion Sci. Technol.*, 71 (2017); http://dx.doi.org/10.13182/FST16-111

37. C. S. Becquart, C. Domain, U. Sarkar, A. DeBacker and M Hou, "Microstructural Evolution of Irradiated Tungsten: Ab Initio Parameterisation of an OKMC Model," *J. Nucl. Mater.*, 403, 1, 75 (2010); http://dx.doi.org/10.1016/j.jnucmat.2010.06.003